IEEE Access
Multidisciplinary | Rapid Review | Open Access Journal

Received April 27, 2020, accepted May 8, 2020, date of publication May 12, 2020, date of current version June 1, 2020.

Digital Object Identifier 10.1109/ACCESS.2020.2994085

Electrical Contact Resistance of Contact Bodies With Cambered Surface

WANBIN REN, (Member, IEEE), CHAO ZHANG, AND XILAI SUN
School of Electrical Engineering and Automation, Harbin Institute of Technology, Harbin 150001, China

Corresponding author: Wanbin Ren (renwanbin@hit.edu.cn)

This work was supported by the National Natural Science Foundation of China under Contract 51377029 and Contract 51777039.

ABSTRACT The electrical contact resistance of cambered surface contact is systematically studied by analytical solution and finite-element simulation. Two representative cambered surface contacts, namely sphere-plane contact and cylinder-plane contact are built and the distributions of electrical current lines profile and isopotential are compared explicitly. Subsequently, the effects of size parameters of cambered surface and mechanical load on contact resistance are evaluated over a large range of aspect ratios. Furthermore, dissimilarity between sphere-plane contact and cylinder-plane contact is deduced.

INDEX TERMS Electrical contact resistance, cambered surface, finite-element (FE) method, electrical current line.

I. INTRODUCTION

Electrical contact, namely a current transferring from one metal to another member through the interface, has always been an important part of the electro-mechanical devices, including but not limited to electromagnetic relays [1], automotive connectors [2], circuit-breakers [3], micro-electro-mechanical systems (MEMS) [4], thin-film devices [5], and switchgears [6]. The electrical current lines would be sharply distorted and bundle together to pass through the contact interface due to the limited contact region[6]. Thus, the additional resistance causing by the shrinking current lines is called constriction resistance, which is a main component of electrical contact resistance between mental contact pairs. Low and stable contact resistance is a fundamental requirement of any electrical and electronic engineering [7]–[10].

The size-dependent contact resistance contains Holm resistance and Sharvin resistance for the large and small contact sizes relative to the mean free path of electron, respectively [11]. When the radius of constriction region a is larger than average electron mean free path λ, Holm has shown that the constriction resistance between two semi-infinite bodies separated by a single circular a-spot could be written as [12]

$$R_H = \frac{\rho_1 + \rho_2}{4a} \tag{1}$$

where ρ_1 and ρ_2 are the electrical resistivity of the contacting conductors. On the other hand, when the radius of constriction region a is comparable or even smaller than the average electron mean free path λ, the constriction resistance is dominated by the Sharvin mechanism and could be expressed by [11]

$$R_S = \frac{p_F}{N\pi e^2 a^2} \tag{2}$$

where p_F, N, and e are Fermi momentum of electrons, electron density, and electron charge, respectively. It is noted that the contact resistance is closely related to the contact radius no matter for which conductive mechanism. And the contact radius is directly determined by the mechanical stress and deformation between two solid surfaces during contact process.

Contact bodies which have dissimilar profiles are said to be non-conforming. The non-conforming contact, including sphere-sphere contact, sphere-plane contact, cylinder-cylinder contact and cylinder-plane contact, is universal and practical in electrical contact application [13], [14]. Many researchers and research institutions have devoted much effort to studying the contact stress distribution [15]–[18], electrical contact resistance [19], [20] and thermal contact resistance [21]–[25] of non-conforming contact. Hertz presented the earliest results about the contact radius calculation for such non-conforming contact [26], which could greatly facilitate the practical application of constriction resistance model. Many valuable works focus on

The associate editor coordinating the review of this manuscript and approving it for publication was Su Yan.

the effects of contact asperity shape and paralleled multi-spot on contact resistance [27]–[33].

Meanwhile, the stresses are highly concentrated in the region close to the contact zone, and the limited contact zone could further increase the constriction resistance. When the profiles of the contact bodies are conforming in one direction and non-conforming in the perpendicular direction, the contact form would evolve into the line contact and the contact zone changes from circular shape to rectangular, which could considerably ease the concentrated stress and effectively enlarge the contact area. Johnson [13] and Hamrock [34] originally analyzed the elastic cylindrical case and provided explicit solutions in their context. Sano deduced the constriction resistance of cylindrical contact and analyzed the effects of space angle [35]. Aichi and Tahara found that the contact resistance of rectangular a-spot is in inverse proportion to the 0.7th and 0.3th power of the contact area with parameters of contact width and length, respectively [36]. Jackson also presented a finite element model of elasto-plastic cylindrical contact and carried out simulations for a range of material properties [37], [38]. However, what condition could minimize the contact resistance of two typical non-conforming contacts remains unexamined.

In addition, the cambered surface contact also exactly exists between the rough surfaces. For the sake of simplicity, many researchers utilize the spherical contact to simulate the single asperity contact. Greenwood and Williamson [39] first presented the contact model for rough surfaces and assumed that all asperities whose heights conform to the Gaussian random distribution have identical curvature radius. And many meaningful works make the asperities equivalent to the spheres with different curvature radius to simulate accurately and analyze the contact situation [40]–[43]. However, there are not only spherical contact but also cylindrical contact in the real contact between rough surfaces according to other researches [44], [45]. Therefore, it is necessary to investigate the effects of aspect ratios and mechanical load on spherical contact and cylindrical contact in the micro scale, which is also the basis of accurate equivalence for rough surface contact.

In a previous paper by the present authors, variations in contact resistance as a function of contact load between rod and spring contacts are investigated explicitly [46]. There is also a remarkable transition stage from spherical contact to cylindrical contact before stable contact. And this could be attributed to the rough surfaces of contact pairs. If the problems mentioned above are solved, then the profile of asperities could be easily estimated in the contact process according to the relationship between contact resistance and contact load. In order to avoid the probable mixture of contact forms caused by the rough surfaces under low contact load, the theoretical solution and finite-element method are employed to further investigate the similarity and difference between cambered surface contacts.

In this paper, the classical sphere and cylinder are selected as two contact bodies with cambered surface,

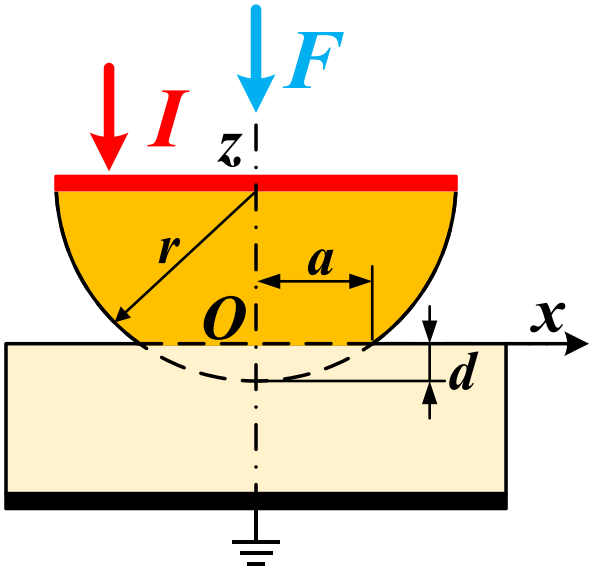

FIGURE 1. The schematic front view for both the sphere-plane contact and cylinder-plane contact.

and then the theoretical solution of contact resistance (only including Holm resistance) for sphere-plane contact and cylinder-plane contact under elastic deformation are presented. Next, the corresponding simulation models for the electrical field analysis by using COMSOL Multiphysics commercial software are built. Then, the isopotential and electrical current lines distribution are obtained for evaluating the conductive ability. Finally, the effects of size parameters and mechanical load on contact resistance are compared explicitly.

II. THEORETICAL SOLUTION

The system of interest and associated size parameters are described schematically in relation to Fig.1. We consider the simple situation of cambered surface with curvature radius r contacting with the plane under mechanical load F, and the indentation depth is d and contact width is $2a$. Then, the current flows inside the half circle, converging toward the center of the joint region with contact radius (half-width), and feeds into the half space connected with electrical ground. For sphere-plane contact, corresponding to the case where the pattern in Fig.1 rotates on the vertical center axis z, the constriction area is a circle shown in Fig.2(a). According to classical Hertz theory, when an elastic semi-sphere is in contact with an elastic plane, the relationship between mechanical load F and indentation depth d could be expressed by [14]

$$F = \frac{4}{3} E r^{1/2} d^{3/2} \tag{3}$$

where $E = [(1 - v_1^2)/E_1 + (1 - v_2^2)/E_2]^{-1}$ is a constant consisting of Young's modulus and Poisson's ratio of the involved materials. And the critical indentation depth $d_{c-\text{sphere}}$ at the

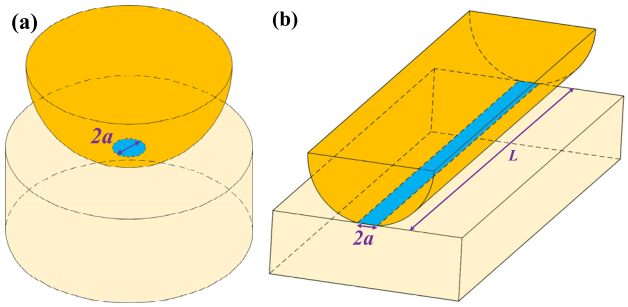

FIGURE 2. 3-D contact models. (a) Sphere-plane contact. (b) Cylinder-plane contact.

end of the elastic deformation is [17]

$$d_{c-sphere} = r(\frac{\pi KH}{2E})^2 \tag{4}$$

where $K = 0.454 + 0.41v$ is the hardness coefficient and H is the hardness of the softer material. When $d \leq d_c$, the deformation between contact pairs is purely elastic. The relationship between contact radius a and curvature radius r of the sphere is shown as $r^2 = a^2 + (r-d)^2$. And the contact radius could be estimated to be $a \approx (rd)^{1/2}$ due to the ratio of $d/a \ll 1$. Substituting this into (3), the contact radius a for sphere-plane contact could be written as

$$a = (\frac{3Fr}{4E})^{1/3} \tag{5}$$

Substituting (5) into (1), the relationship between contact resistance $R_{\mathrm{c-sphere}}$ of sphere-plane contact and mechanical load F is as follows

$$R_{\mathrm{c-sphere}} = \rho(\frac{E}{6r})^{1/3}F^{-1/3} \tag{6}$$

As for cylinder-plane contact, corresponding to the case where the pattern in Fig.1 is symmetrical about the vertical center axis z, the constriction area is a rectangle with contact length L in the third, ignorable dimension which is perpendicular to the paper shown in Fig.2(b). When an elastic semi-cylinder contacts with an elastic plane, the relationship between mechanical load F and indentation depth d during elastic deformation could be described by [14]

$$F = \frac{\pi}{4}ELd \tag{7}$$

Similarly, the critical indentation depth $d_{\mathrm{c-cylinder}}$ for cylinder-plane contact at the end of the elastic deformation could be expressed by

$$d_{c-cylinder} = 2r(\frac{KH}{E})^2 \tag{8}$$

And the contact half-width could also be estimated to be $a \approx (rd)^{1/2}$. Substituting this into (7), the contact half-width a for cylinder-plane contact is obtained

$$a = (\frac{4Fr}{\pi EL})^{1/2} \tag{9}$$

The contact resistance of a rectangular a-spot could be written as [35]

$$R_{\mathrm{c-cylinder}} = \frac{2\rho}{\pi L}\ln\frac{2r+\sqrt{a^2+(2r)^2}}{a} \tag{10}$$

When considering the ratio of $a/2r \ll 1$ in the normal case, (10) could be simplified by

$$R_{\mathrm{c-cylinder}} = \frac{2\rho}{\pi L}\ln\frac{4r}{a} \tag{11}$$

Substituting (9) into (11), the relationship between contact resistance $R_{\mathrm{c-cylinder}}$ of cylinder-plane contact and mechanical load F is as follows

$$R_{\mathrm{c-cylinder}} = \frac{\rho}{\pi L}\ln\frac{4\pi ELr}{F} \tag{12}$$

According to (5) and (9), the contact radius in the contact region is not only related to the size parameters of contact bodies, such as curvature radius and contact length, but also dependent on the contact load between contact pairs. And the conductive mechanism is directly determined by the magnitude of contact radius. It has been experimentally validated that the conductive mechanism is Sharvin-type dominantly at low load, and transits to Holm-type with the load increasing [47], [48]. In this paper, only the Holm resistance is considered and investigated under different combinations of size parameters and contact load. Thus, the analytical model mentioned above and the following conclusions are more suitable when the actual contact radius is larger than the average electron mean free path comprehensively.

III. FINITE ELEMENT MODELING FOR ELECTRICAL FIELD ANALYSIS

To visualize the isopotential and electrical current lines distribution of sphere-plane contact and cylinder-plane contact for various combinations of a, r and L, the commercial program COMSOL Multiphysics 5.3a version is used to perform simulations by solving electric field equations through FEM. The contact pairs are set as pure copper material whose electrical resistivity is $1.65 \times 10^{-8}\Omega$·m, typical Young's modulus is $E_1 = E_2 = 115 \times 10^9$ Pa, hardness is $H = 900$ N/mm^2 and Poisson's ratio is $v_1 = v_2 = 0.33$ [6]. Both the 3D contact problem of sphere-plane and cylinder-plane could be simplified to the 2D plane strain problem as shown in Fig.3(a) according to the symmetry property. And the selected space dimensions in COMSOL Multiphysics 5.3a are 2D axisymmetric and 2D for sphere-plane and cylinder-plane contacts, respectively. Then, in Solid Mechanics interface, the z-axis is defined as the symmetry axis for sphere-plane contact, while two vertically left edges are defined as symmetry boundaries for cylinder-plane contact with an extension in the perpendicular direction. Thus, a quarter of cambered surface with curvature radius $r_0 = 1$mm and a square with size of 1×1mm^2 and $L_0 = 2r_0 = 2$mm in the perpendicular direction specially for cylinder-plane contact are built and meshed with traditional triangular elements in Fig.3. The meshes, presented in Fig.3, are graded radially outward from the

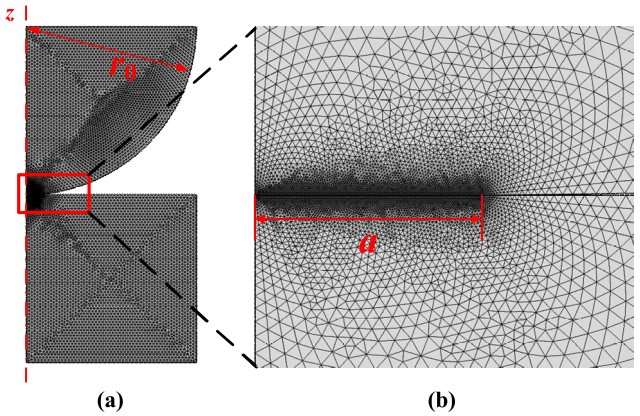

FIGURE 3. 2-D model with COMSOL Multiphysics. (a) Illustration of model with mesh. (b) Zoomed-in view of the mesh around the contact region and contact half-width a is 10μm.

initial point of contact, with the densest mesh in the contact region. A series of mesh convergence studies are conducted and the maximal size of the mesh around the contact region is determined as 0.07μm. This means that the simulated contact resistance results are not affected with the size of the mesh further decreasing. And the contact surfaces are assumed smooth. Electrically, a prescribed constant current 10mA is applied to the top-most surface and the bottom-most surface is electrically grounded. Axis symmetry on the leftmost boundary results in electrical insulation. The lateral surfaces of both bodies are also considered electrically insulated. For better description, the Laplace equation and boundary conditions for sphere-plane and cylinder-plane contact are described with the cylindrical and Cartesian coordinates, respectively. The corresponding distribution of the potential φ for sphere-plane and cylinder-plane contact are written as

$$\frac{1}{r}\frac{\partial}{\partial r}(r\frac{\partial \varphi}{\partial r})+\frac{\partial^2 \varphi}{\partial z^2}=0 \tag{13}$$

$$\frac{\partial^2 \varphi}{\partial x^2}+\frac{\partial^2 \varphi}{\partial z^2}=0 \tag{14}$$

And the boundary conditions for sphere-plane and cylinder-plane contacts both could be described as follows

$$\frac{\partial \varphi_1}{\partial z}=\rho_1 J_0, 0\le r\le r_0, z=r_0 \tag{15}$$

$$\frac{\partial \varphi_1}{\partial l}=0, l=\sqrt{(z-r_0)^2+x^2}, a\le r\le r_0, 0\le z\le r_0 \tag{16}$$

$$\rho_2\frac{\partial \varphi_1}{\partial z}=\rho_1\frac{\partial \varphi_2}{\partial z}, 0\le r\le a, z=0 \tag{17}$$

$$\frac{\partial \varphi_2}{\partial z}=0, a\le r\le r_0, z=0 \tag{18}$$

$$\frac{\partial \varphi_2}{\partial x}=0, r=r_0,\ 0\le z\le r_0 \tag{19}$$

$$\varphi_2=0, 0\le r\le a, z=0 \tag{20}$$

where the current density are $J_0=I_0/(\pi r_0^2)$ and $J_0=I_0/(2r_0L)$ for sphere-plane and cylinder-plane contacts, respectively, due to the circular and rectangular top-most surface.

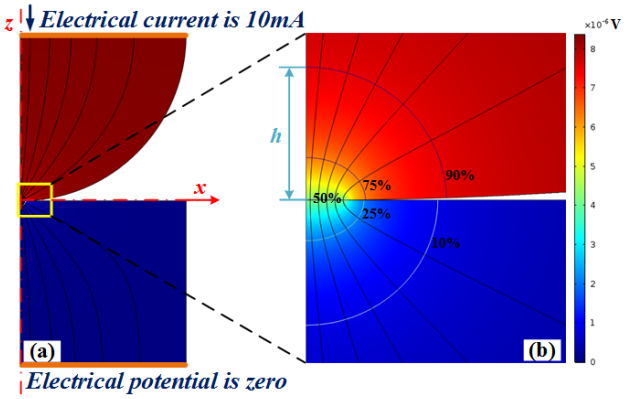

FIGURE 4. Distributions of electrical current lines and isopotential of sphere-plane contact. (a) Electrical current lines profile and isopotential maps of the whole region. (b) Zoomed-in view of results around the contact region.

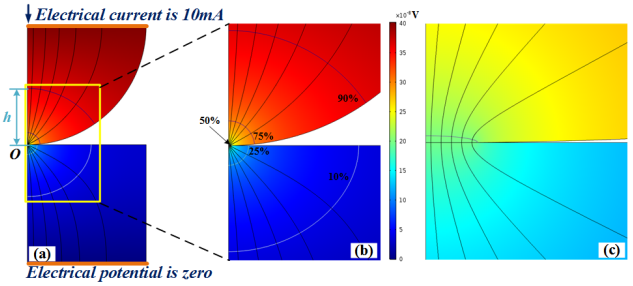

FIGURE 5. Distributions of electrical current lines and isopotential of cylinder-plane contact. (a) Electrical current lines profile and isopotential maps of the whole region. (b) Zoomed-in view of results around the contact region. (c) Zoomed-in view of (b).

The simulation results of isopotential maps and electrical current lines profile at 10mA electrical current load are shown in Fig.4 and Fig.5 for sphere-plane contact and cylinder-plane contact, respectively. As expected, the current lines are orthogonal to the potential lines and shrink uniformly radially toward the contact region. And the distribution of current lines are densest around the vicinity of the contact region. It is necessary to investigate the electrical potential distribution on the top-most surface in order to illustrate whether the half-sphere with limited height of $r_0=1$mm in finite-element model has influence on the constriction of current lines. The height h is defined as the vertical distance from the horizontal line to the contact region. And the potential distribution on the horizontal lines with different heights from 0.5mm to 1mm are shown in Fig.6. It is noted that the electrical potential increases significantly from 8.25 μ V to 8.275 μ V along the horizontal line away from the vertical z-axis for $h=0.5$mm. And the variations of electrical potential becomes smaller with the height h increasing until all potential are equal for $h=1$mm corresponding to the top-most surface. This means that the top-most surface is an isopotential surface even under limited height. For better description, the isopotential lines corresponding to $90\%U$, $75\%U$, $50\%U$, $25\%U$ and $10\%U$ are drawn in Fig.4 and Fig.5, where U is the electrical potential of the top-most surface.

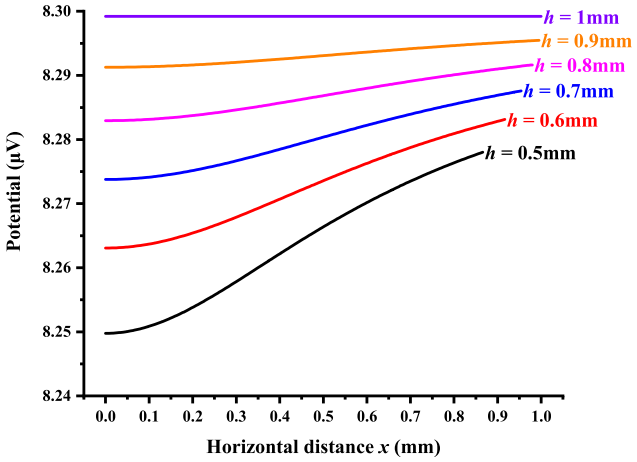

FIGURE 6. The electrical potential distribution on the horizontal lines with different heights h from 0.5mm to 1mm.

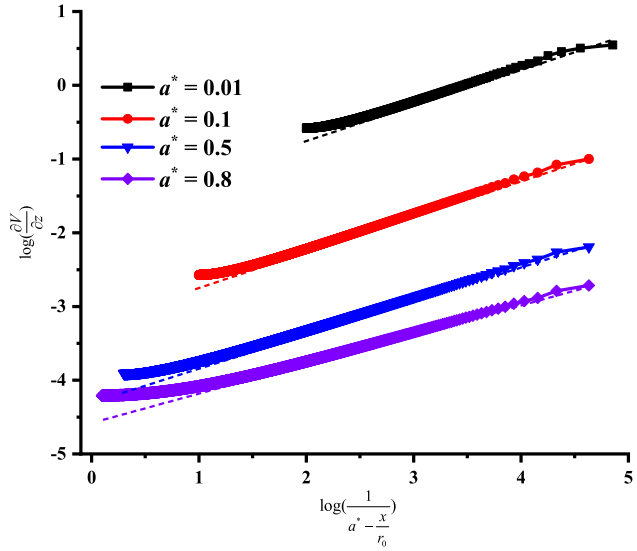

FIGURE 7. Variations of $\log(\partial V/\partial z)$ as a function of $\log[1/(a^* - x/r_0)]$ with different normalized contact half-width a^* of 0.01, 0.1, 0.5 and 0.8. The dashed lines are the asymptotes.

It is obvious that the electrical potential decreases sharply especially around the contact region for both two contact structural configurations, which means that the decreasing potential mainly concentrates around the interface.

Then a local analysis is used to investigate the singularity in the partial derivative of voltage with respect to the vertical axis along the edge of contacts, which is arose due to the mixed boundary condition at $(a, 0)$. To confirm that finite-element analysis captures the singularity behavior, $\log(\partial V/\partial z)$ against $\log[1/(a^* - x/r_0)]$ with different normalized contact half-width a^* of 0.01, 0.1, 0.5 and 0.8 are plotted in Fig.7. When x/r_0 is close to a^* from the negative direction, $\log(\partial V/\partial z)$ increases along the straight line asymptotically. This phenomenon conforms to the associated singularity behavior mentioned in Ref [49]. And this indicates that FEA correctly captures the singularity behavior at $(a, 0)$.

The normalized height is written by $h^* = h/r$ to eliminate the influence of the curvature radius of cambered surface.

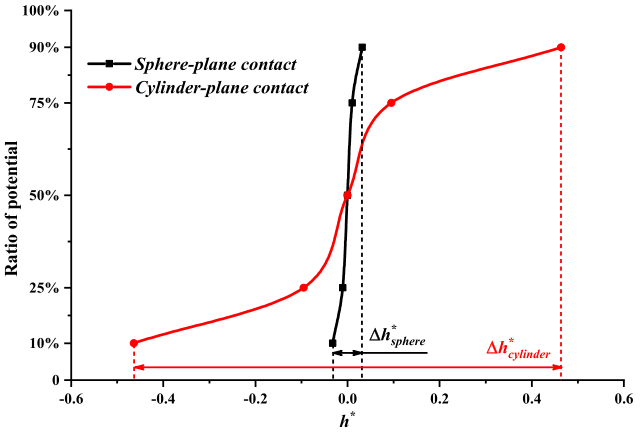

FIGURE 8. The ratio of potential as a function of normalized height h* for curvature radius r = 1mm, contact half-width a = 10um and contact length L = 2mm for sphere-plane and cylinder-plane contact.

Fig.8. shows the results of the ratio of potential as a function of the obtained normalized height h^*. As seen, when the percent of potential drops from 90% to 75% then to 50%, the normalized height h^* decreases from 0.032 to 0.01 then to 0 for sphere-plane contact and decreases from 0.46 to 0.09 then to 0 for cylinder-plane contact. Thus, the decreasing rate of the potential of sphere-plane contact is always faster than that of cylinder-plane contact. So the former has a slower decline rate of potential along the arc profile than the latter and the same isopotential line is closer to the contact region for the fixed ratio of potential. The normalized relative height of the constriction region is defined as $\Delta h^* = \Delta h/r = (h_{90\%U} - h_{10\%U})/r$ for evaluating the ability to confine current for different contact configurations. And the normalized relative height Δh^* are 0.064 and 0.93 corresponding to sphere-plane and cylinder-plane contacts in Fig.8. This indicates that the sphere-plane contact has a narrower constriction region and a stronger current crowding ability than cylinder-plane contact.

IV. RESULTS AND DISCUSSION

A. EFFECT OF NON-CONFORMING CONTACT WIDTH

The normalized contact resistance R_c^* is defined uniformly as

$$R_c^* = \frac{R_c}{\frac{\rho}{2r}} \tag{21}$$

where R_c could represent the contact resistance for either $R_{c-sphere}$ or $R_{c-cylinder}$ and $\rho/2r$ is the reference value of normalization.

Fig.9 shows the results of illustrative calculations of the dependence of R_c^* on the normalized contact half-width a/r with curvature radius of $r = 1$mm and varied normalized cylinder-plane length L/r from 0.01 to 100 by using (1), (10) and (21) for sphere-plane contact and cylinder-plane contact, respectively. The contact resistance drops linearly and steeply for sphere-plane contact with a constant index $m = 1$ in logarithmic coordinates. For cylinder-plane contact, the contact resistance rises significantly with the shortening of cylindrical length L. And the fitting results for different contact length L in Fig.9 uniformly show that the relationship

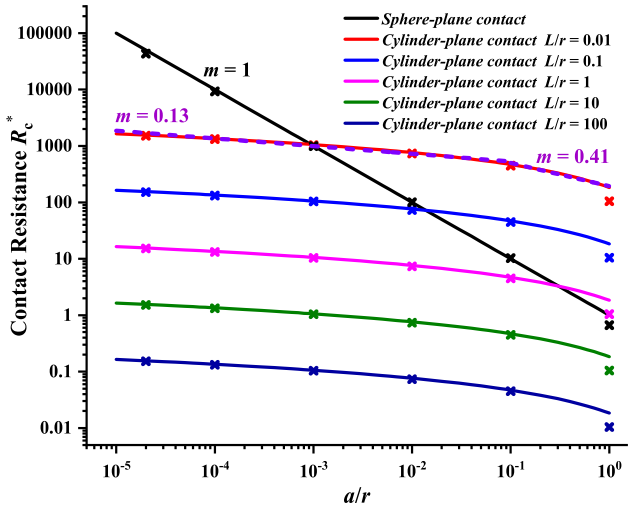

FIGURE 9. The normalized contact resistance R_c^* as a function of normalized contact half-width a/r (r = 1mm) with varied contact length L/r. The continuous lines represent the theoretically calculated contact resistance by (1) and (10). And the discrete crosses are the simulated results for the given contact radius.

between the normalized contact resistance R_c^* and normalized contact half-width a/r could be taken as the power function $R_c^* = K_1(a/r)^{-m}$ and the index m is calculated as 0.13 and 0.41, for the case of $a/r \leq 0.1$ and $a/r > 0.1$, respectively.

The simulation results (crosses) of sphere-plane contact and cylinder-plane contact are also included in Fig.9. It is clear that the simulations are in excellent agreement with the analytical calculations for the values of a/r from 0.00001 to 0.1. When $a/r = 0.1$, the absolute difference value between simulation and analytical results for cylinder-plane contact is only 0.23 mΩ. However, the appreciable deviation 0.87 mΩ is observed for $a/r \approx 1$. The larger deviation between the analytical and simulation results when the normalized contact half-width a/r is close to 1 could be attributed to the fact that the ratio of a/r does not satisfy the application assumption of $a/r \ll 1$. Then (1) and (10) would always overestimate the constriction resistance for sphere-plane and cylinder-plane contacts when the ratio of a/r tends to be 1. Thus, the analytical results of constriction resistance for sphere-plane and cylinder-plane contacts are believable when $a/r \leq 0.1$.

Fig.10 and Fig.11 show the electrical current lines profile in the right half of circle (shown in Fig.1) with various contact half-width a/r by using FEM for sphere-plane contact and cylinder-plane contact, respectively. As shown, the distributions of current lines are similar for two different contact structures with the same a/r, which is determined by the same shape feature in the non-conforming direction (shown in Fig.1). The current lines are horizontally crowded around the contact region when $a/r = 0.01$ corresponding to a smaller contact half-width as shown in Fig.10(a) and Fig.11(a), since in this limit most of current lines are restricted and flow along the arc profile towards the constriction region, which causes a larger contact resistance. Then, the current lines become vertically crowded as shown in Fig.10(d) and Fig.11(d) when $a/r = 0.1$,

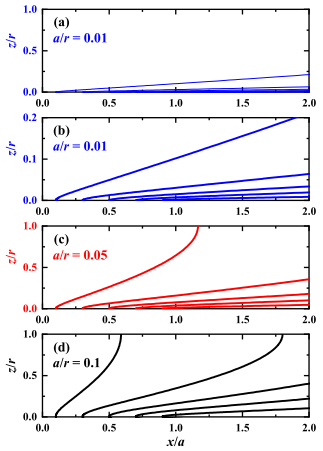

FIGURE 10. Distribution of electrical current lines of sphere-plane contact with (a) a/r = 0.01 (r = 1mm), (b) zoom in view of (a) for 0 ≤ z/r ≤ 0.2, (c) a/r = 0.05, and (d) a/r = 0.1.

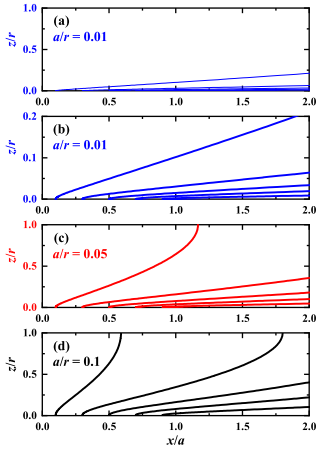

FIGURE 11. Distribution of electrical current lines of cylinder-plane contact for L/r = 10 (r = 1mm) with (a) a/r = 0.01, (b) zoom in view of (a) for 0 ≤ z/r ≤ 0.2, (c) a/r = 0.05, and (d) a/r = 0.1.

since the effectively conductive region increases with the contact half-width lengthening and the current lines become less dense, which is corresponding to a smaller contact resistance.

The height distributions of various isopotential with $90\%U$, $75\%U$, $50\%U$, $25\%U$ and $10\%U$ for sphere-plane contact and cylinder-plane contact are shown in Fig.12. The normalized height h^* and the relative height of the constriction region Δh^* decrease significantly with the normalized contact half-width a/r decreasing. This means that a smaller contact half-width corresponds to a narrower conductive region, and further prevents the electrical current to pass through.

B. EFFECT OF CONFORMING CONTACT LENGTH

Fig.13 shows the relationship between normalized contact resistance R_c^* and normalized contact length L/r with varied normalized contact half-width a/r from 0.01 to 0.1 by using (1), (10) and (21). As shown, the normalized contact resistance of cylinder-plane contact decreases linearly with increasing L/r, i.e., with increasing value of L for a fixed value of r, in logarithmic coordinates. This means that the

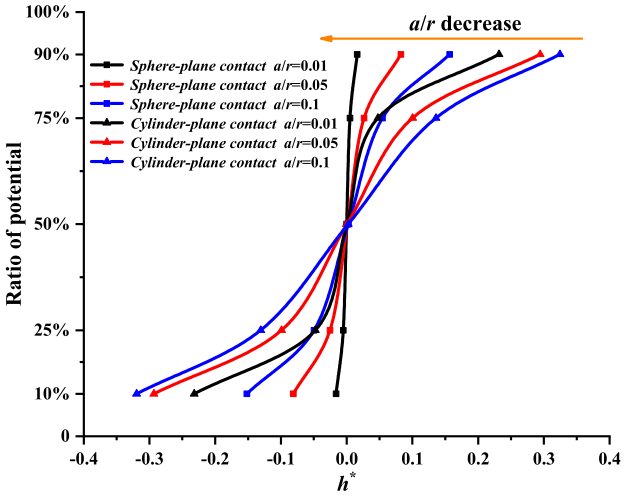

FIGURE 12. The ratio of potential as a function of normalized height h* with varied a/r = 0.01, 0.05 and 0.1 for sphere-plane contact and cylinder-plane contact.

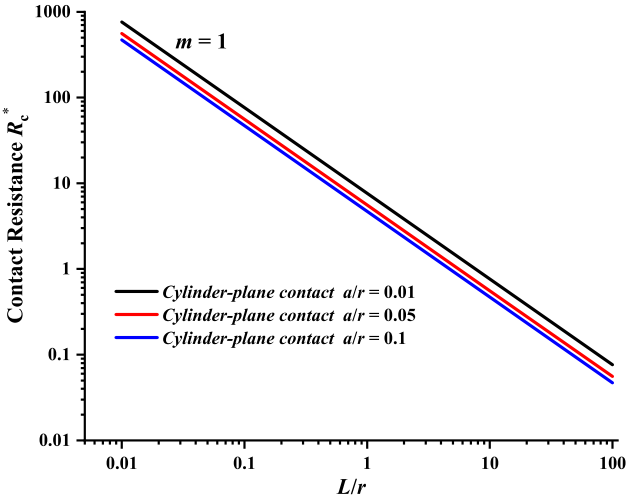

FIGURE 13. Variations of normalized contact resistance R_c^* versus the ratio of L/r with varied contact half-width a/r.

variation of contact resistance for cylinder-plane contact is dependent on the normalized contact length L/r.

Interestingly, the distributions of the current lines profile and isopotential are the same with identical contact half-width a and varied contact length L. Thus, the curves of current lines profile and isopotential in Fig.10 and Fig.11 consist of many values of L/r. So distribution of field lines and isopotential maps is independent of contact length L. When the normalized contact half-width $a/r \leq 0.1$, the normalized contact resistance R_c^* decreases with the index of 0.13 and 1 with increasing a/r and L/r, respectively. So the data from the calculation results allow us to synthesize simple scaling law for normalized contact resistance R_c^* of cylinder-plane contact as

$$R_c^* = 3.85(\frac{a}{r})^{-0.13}(\frac{L}{r})^{-1} \ (a/r \leq 0.1) \tag{22}$$

The maximum of relative difference is only about 9% between the calculations of (11) and (22). And the

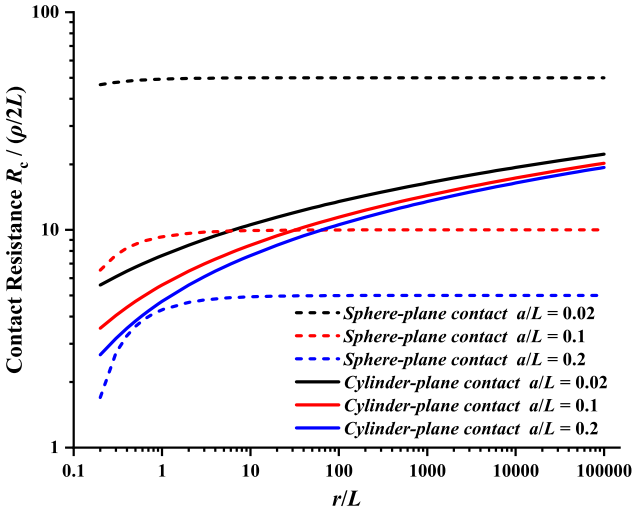

FIGURE 14. Variations of contact resistance $R_c/(\rho/2L)$ versus the ratio of r/L (L = 0.5mm) with varied contact half-width a/L.

obtained (22) shows a concise relationship among normalized contact resistance R_c^*, normalized half-width a/r and normalized contact length L/r for cylinder-plane contact. As seen, (22) indicates that the influences of normalized half-width a/r and normalized contact length L/r on contact resistance are independent. And the variation of contact resistance conforms to two power laws with varied a/r and L/r for cylinder-plane contact compared with only one for sphere-plane contact in (1). This difference is mainly attributed to the fact that the sphere-plane contact is non-conforming in any directions, while the cylinder-plane is non-conforming along the contact half-width a only.

C. EFFECT OF CAMBERED CURVATURE RADIUS

It is conditionally correct for the simplified calculation of (1) for the circular a-spot when the contact radius a is far smaller than the curvature radius r. To study the influence of curvature radius on the contact resistance for sphere-plane contact, the contact resistance is accurately given as [50]

$$R_{c-sphere} = (\frac{\rho}{2a})[1 - 1.41581(\frac{a}{r}) + 0.06322(\frac{a}{r})^2 + 0.15261(\frac{a}{r})^3 + 0.19998(\frac{a}{r})^4] \tag{23}$$

The calculation results of the dependence of $R_c/(\rho/2L)$ on the normalized curvature radius r/L with varied normalized contact half-width a/L from 0.02 to 0.2 by using (11) and (23) for cylinder-plane contact and sphere-plane contact are shown in Fig.14. For sphere-plane contact case, the factor of a/L and r/L entirely dominates the variations of $R_c/(\rho/2L)$. Specially, the contact resistance tends to be constant when $r/L > 10$. For cylinder-plane contact case, it is noticed that the increase of contact resistance mainly depends on the factor of r/L. When the factor of r/L is larger than 30 and $a/L = 0.1$, the resistance becomes increasingly higher than that of sphere-plane contact.

Fig.15 and Fig.16 show the electrical current lines profile in the right half of circle (shown in Fig.1) with various

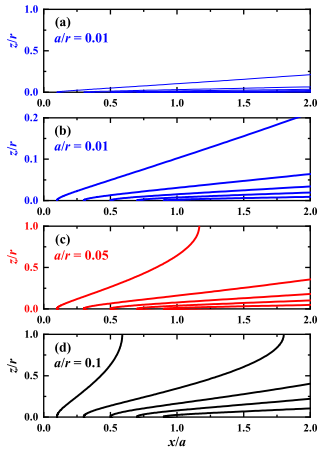

FIGURE 15. Distributions of electrical current lines of sphere-plane contact for a/L =0.1 with (a) r/L = 0.1, (b) r/L = 1, (c) r/L = 10, and (d) r/L = 100.

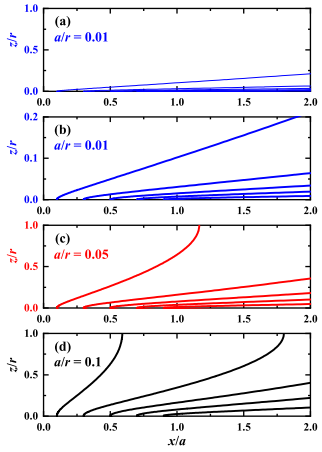

FIGURE 16. Distributions of electrical current lines of cylinder-plane contact for a/L =0.1 with (a) r/L = 0.1, (b) r/L = 1, (c) r/L = 10, and (d) r/L = 100.

curvature radius of cambered surface r/L by means of FEM for sphere-plane contact and cylinder-plane contact, respectively. The current lines are vertically crowded around the contact region, which are almost parallel to the vertical center axis, when $r/L = 0.1$ as shown in Fig.15(a). This is attributed to the half sphere approaching to a cylinder whose center axis is vertical to the contact region due to the curvature radius decreasing. Therefore, the effect of confining current becomes weaker and the current lines are vertical to the contact region which decreases contact resistance. Then, the current lines become horizontally crowded around the contact region when $r/L = 100$ as shown in Fig.15(d), which is caused by the current lines flowing along the profile of the sphere due to the larger curvature radius. The distribution of current lines of cylinder-plane contact is similar to that of sphere-plane contact, which is also from vertically crowded to horizontally crowded with increase of curvature radius of cylinder.

The height distributions of various isopotential with $90\%U$, $75\%U$, $50\%U$, $25\%U$ and $10\%U$ with varied curvature radius r/L from 0.1 to 10 for sphere-plane contact and

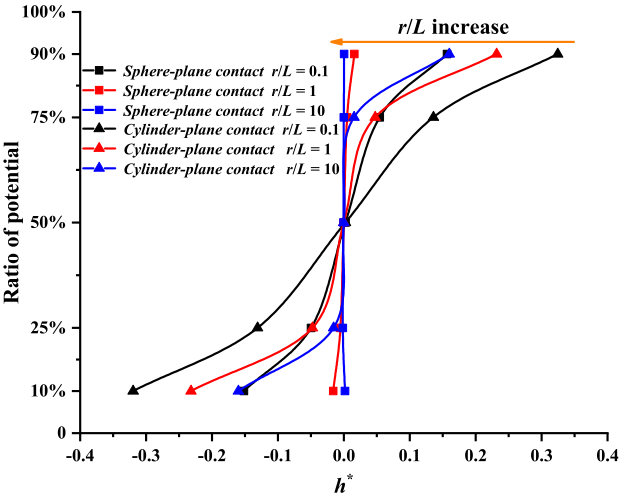

FIGURE 17. The ratio of potential as a function of normalized height h* with varied normalized curvature radius of cambered surface r/L = 0.1, 1 and 10.

cylinder-plane contact are shown in Fig.17. The normalized height h^* and the relative height of the constriction region Δh^* both decrease significantly with the normalized curvature radius increasing. For the fixed isopotential, the parameters h^* and Δh^* of sphere-plane contact are always lower than that of cylinder-plane contact, which indicates that the isopotential distribution of former is closer to the contact a-spot than the latter. So the crowding ability for electrical current of cylinder-plane is weaker than that of sphere-plane contact, and there would be a lower potential difference for cylinder-plane contact corresponding to a smaller contact resistance. However, the potential decreases significantly for cylinder-plane contact along the arc profile of cylinder, which causes a larger bulk resistance. And the bulk resistance would increase with the curvature radius of cylinder increasing. This is the root reason for a larger resistance for cylinder-plane contact with the curvature radius increasing than that of sphere-plane contact.

D. ROLE OF MECHANICAL LOAD

To further probe into the variation law of contact resistance versus mechanical load, the size parameters (contact half-width a and contact length L) and mechanical load F are normalized by the curvature radius r and all dimensionless parameters are denoted with an asterisk. The relationship between the normalized contact resistance R_c^* and normalized mechanical load F^* for sphere-plane contact according to (1), (5) and (21) is

$$R^*_{\text{c-sphere}} = (\frac{3}{4}F^*)^{-1/3} \tag{24}$$

where the normalized mechanical load is defined as $F^* = F/(Er^2)$. And for cylinder-plane contact, according to (9), (21) and (22), when $a/r \leq 0.1$, the relationship between the normalized contact resistance R_c^* and normalized mechanical load F^* could be written by

$$R^*_{\text{c-cylinder}} = 3.79(L^*)^{-0.935}(F^*)^{-0.065} \tag{25}$$

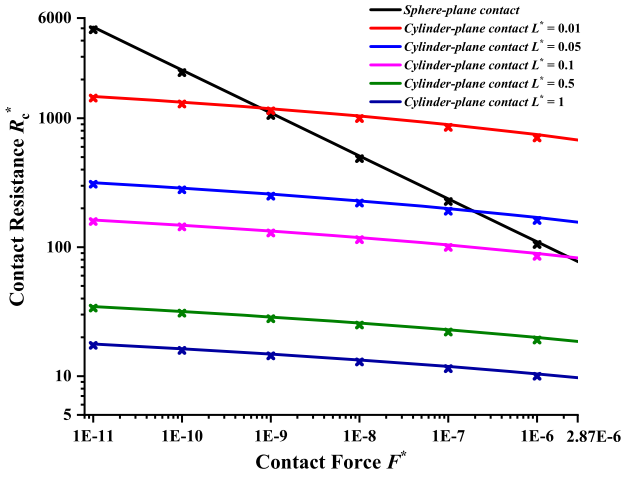

FIGURE 18. The normalized contact resistance R_c^* as a function of normalized mechanical load F* with varied normalized contact length L*. The continuous lines represent the theoretically calculated contact resistance by (24) and (25). And the discrete crosses are the simulated results for the given contact.

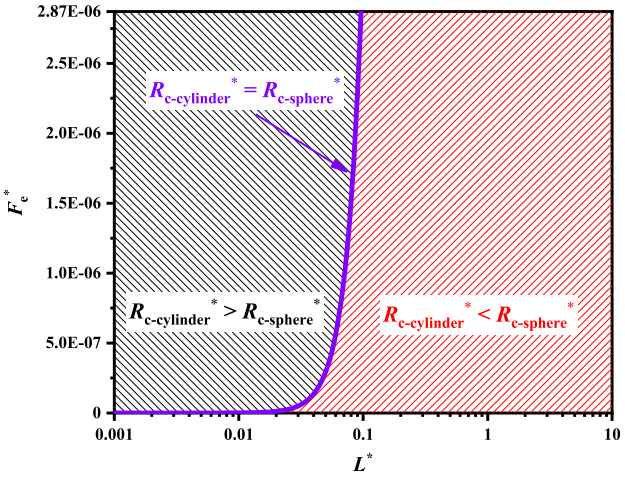

FIGURE 19. Contact resistance comparison maps of contact bodies with cambered surface based on normalized mechanical load F_e^* and normalized contact length L*.

where the normalized contact length is defined as $L^* = L/r$. Fig.18 shows the results of illustrative calculations of the dependence of normalized contact resistance R_c^* on the normalized mechanical load F^* with curvature radius $r = 1$mm and varied normalized cylindrical length L^* from 0.01 to 100 by using (24) and (25) when the normalized contact half-width $a^* \leq 0.1$. The normalized contact resistance R_c^* decreases with index $m = 0.33$ for sphere-plane contact with the normalized mechanical load F^* increasing. However, for cylinder-plane contact, R_c^* decreases with index $m = 0.935$ and 0.065 with the normalized contact length L^* and normalized mechanical load F^* increasing. This indicates that mechanical load has slight influence on the contact resistance compared with contact length for cylinder-plane contact. In order to make the analytical results convincible and validate the simplification of the Hertzian contact area under the effect of mechanical load, the electro mechanical coupling simulations are also conducted by COMSOL Multiphysics 5.3a. And the vertical prescribed displacement is progressively applied on the top-most surface of the half-sphere in Fig.3(a). The produced contact loads and contact resistance are calculated after the whole simulation progress. The simulation results (crosses) of sphere-plane contact and cylinder-plane contact are also added in Fig.18. The decrease of normalized contact resistance with the normalized contact load increasing for simulation results in Fig.18 shows a similar trend with lower slope compared to the results in Fig.9. This is caused by the nonlinear increase of contact radius with the contact load increasing as described in (5) and (9). It is obvious that the simulation results are in excellent agreement with the analytical calculations for the values of F^* from 10^{-11} to 10^{-7}. After that, there are larger deviations between analytical and simulation results, which is corresponding to the case of larger contact radius in Fig.9. This could also be attributed that the Hertzian contact radius a derived from (5) and (9) for sphere-plane and cylinder-plane contacts are not valid with the contact radius increasing. Thus $a \approx (rd)^{1/2}$ would underestimate the real contact radius which further cause a larger constriction resistance. Therefore, the electro mechanical coupling technique is necessary to determine the difference in the contact radius and contact resistance between the analytical and simulation results under the mechanical load effect.

According to (24) and (25), the normalized mechanical load F_e^*, which make the contact resistance of sphere-plane contact equal to that of cylinder-plane contact, could be written into

$$F_e^* = 9.97 \times 10^{-3}(L^*)^{3.48} \tag{26}$$

Fig.19 illustrates the variations in normalized mechanical load F_e^* as a function of normalized contact length L^*. It is noted that the calculated critical normalized contact load F^* is equal to 2.87×10^{-6} for the elastic sphere-plane contact, corresponding to the critical indentation depth in (4). Though the critical normalized contact load for cylinder-plane contact varies with the contact length, it is always higher than the F_e^* for the fixed normalized contact length L^*. Thus, the contact resistance map with different maximum normalized contact load is similar for Fig.19. Therefore, the maximum F_e^* is selected as 2.87×10^{-6} in Fig.19 to guarantee the purely elastic deformation and further compare two contact configurations. As shown, the contact resistance of sphere-plane contact is exactly comparable to the resistance of cylinder-plane contact. Such exponential demarcation curve indicates that the resistance difference between sphere-plane contact and cylinder-plane is closely dependent on contact length and mechanical load. Furthermore, the cylinder-plane electrical contact with large contact length is preferable in the low mechanical load engineering application. For instance, the Series J255 TO-5 (Transistor Outline Package) relay could decrease the contact resistance to be lower than 50mΩ under contact load of tens of milli-newton [51]. While the

sphere-plane contact could improve the electrical performance by increasing the mechanical load when the space is limited. And the sphere-plane electrical contact has a great advantage for miniaturization.

V. CONCLUSION

This paper mainly aims to systematically investigate the similarity and difference between two typical cambered surface contacts, i.e. sphere-plane contact and cylinder-plane contact, under the elastic deformation based on the effects of size parameters and mechanical load on the contact resistance. Our results indicate that mechanical load is a sensitive parameter to contact resistance of sphere-plane contact. Meanwhile, the contact resistance of cylinder-plane contact is significantly affected by contact length. This difference is attributed to the fact that the specific conforming feature of cylinder-plane contact. The distributions of simulated constriction region show that the sphere-plane contact has a stronger current crowding ability. And the simplification of the Hertzian contact area for both sphere- and cylinder-plane contacts is limited with larger contact radius for $a/r > 0.1$. Furthermore, the conductive ability of non-conforming contact is determined by the feature of cambered surface and mechanical load comprehensively. And the superiority of cylinder-plane contact would be performed even under low mechanical load. This is a positive and beneficial conclusion in engineering applications for electrical contacts, especially for the determination of contact structure in the design process. And the dimensionless results of contact resistance could be instructive to the stable electrical contact for MEMS under smaller dimension and lower contact load. In future, the detailed works on the plastic deformation will be in schedule for comparison to the elastic deformation for different contact structures.

REFERENCES

[1] Z.-K. Chen and G. J. Witter, "Electrical contacts for automotive applications: A review," *IEICE Trans. Electron.*, vol. E87-C, no. 8, pp. 1248–1254, 2004.

[2] C. Farges, M. Chevrie, J. Sabatier, L. Pradere, and F. Guillemard, "Detection of electric contact resistance variations in automotive connectors," *IEEE Trans. Ind. Electron.*, vol. 64, no. 12, pp. 9469–9476, Dec. 2017.

[3] M. Rong, Q. Ma, Y. Wu, T. Xu, and A. B. Murphy, "The influence of electrode erosion on the air arc in a low-voltage circuit breaker," *J. Appl. Phys.*, vol. 106, no. 2, Jul. 2009, Art. no. 023308.

[4] A. Basu, G. G. Adams, and N. E. McGruer, "A review of micro-contact physics, materials, and failure mechanisms in direct-contact RF MEMS switches," *J. Micromech. Microeng.*, vol. 26, no. 10, Oct. 2016, Art. no. 104004.

[5] E. Crinon and J. T. Evans, "The effect of surface roughness, oxide film thickness and interfacial sliding on the electrical contact resistance of aluminium," *Mater. Sci. Eng., A*, vol. 242, nos. 1–2, pp. 121–128, Feb. 1998.

[6] P. G. Slade, *Electrical Contacts: Principles and Applications*. New York, NY, USA: CRC, 2014, pp. 4–11.

[7] M. Braunovic, N. K. Myshkin and V. V. Konchits, *Electrical Contacts: Fundamental Applications and Technology*. London, U.K.: Talor & Francis, 2006.

[8] A. Lumbantobing, L. Kogut, and K. Komvopoulos, "Electrical contact resistance as a diagnostic tool for MEMS contact interfaces," *J. Microelectromech. Syst.*, vol. 13, no. 6, pp. 977–987, Dec. 2004.

[9] M. Abdollah and A. A. Razi-Kazemi, "Intelligent failure diagnosis for gas circuit breakers based on dynamic resistance measurements," *IEEE Trans. Instrum. Meas.*, vol. 68, no. 9, pp. 3066–3077, Sep. 2019.

[10] H. Park, R. Beresford, R. Ha, H.-J. Choi, H. Shin, and J. Xu, "Evaluation of metal–nanowire electrical contacts by measuring contact end resistance," *Nanotechnology*, vol. 23, no. 24, Jun. 2012, Art. no. 245201.

[11] A. Mikrajuddin, F. G. Shi, H. K. Kim, and K. Okuyama, "Size-dependent electrical constriction resistance for contacts of arbitrary size: From sharvin to holm limits," *Mater. Sci. Semicond. Process.*, vol. 2, no. 4, pp. 321–327, Dec. 1999.

[12] R. Holm, *Electric Contacts: Theory and Application*. New York, NY, USA: Springer-Verlag, 1967, pp. 14–16.

[13] K. L. Johnson, *Contact Mechanics*. Cambridge, U.K.: Cambridge Univ. Press, 1985, pp. 109–112.

[14] V. L. Popov, *Contact Mechanics and Friction: Physical Principles and Applications*. New York, NY, USA: Springer, 2010, pp. 13–16.

[15] A. Cinar and G. B. Sinclair, "Quasi-static normal indentation of an elasto-plastic half-space by a rigid circular cylinder of infinite length," *Int. J. Solids Struct.*, vol. 22, no. 8, pp. 919–934, 1986.

[16] I. Green, "Poisson ratio effects and critical values in spherical and cylindrical Hertzian contacts," *Int. J. Appl. Mech. Eng.*, vol. 10, no. 3, pp. 451–462, 2005.

[17] W. R. Chang, I. Etsion, and D. B. Bogy, "An elastic-plastic model for the contact of rough surfaces," *J. Tribol.*, vol. 109, no. 2, pp. 257–263, Apr. 1987.

[18] Y. Zhao, D. M. Maietta, and L. Chang, "An asperity microcontact model incorporating the transition from elastic deformation to fully plastic flow," *J. Tribol.*, vol. 122, no. 1, pp. 86–93, Jan. 2000.

[19] P. Zhang, Y. Y. Lau, and R. M. Gilgenbach, "Thin film contact resistance with dissimilar materials," *J. Appl. Phys.*, vol. 109, no. 12, Jun. 2011, Art. no. 124910.

[20] W. Ren, Y. Chen, Z. Wang, S. Xue, and X. Zhang, "Electrical contact resistance of coated spherical contacts," *IEEE Trans. Electron Devices*, vol. 63, no. 11, pp. 4373–4379, Nov. 2016.

[21] G. Anciaux and J. F. Molinari, "A molecular dynamics and finite elements study of nanoscale thermal contact conductance," *Int. J. Heat Mass Transf.*, vol. 59, pp. 384–392, Apr. 2013.

[22] J. J. Salgon, F. Robbe-Valloire, J. Blouet, and J. Bransier, "A mechanical and geometrical approach to thermal contact resistance," *Int. J. Heat Mass Transf.*, vol. 40, no. 5, pp. 1121–1129, Mar. 1997.

[23] M. Bahrami, M. M. Yovanovich, and J. R. Culham, "Thermal contact resistance at low contact pressure: Effect of elastic deformation," *Int. J. Heat Mass Transf.*, vol. 48, no. 16, pp. 3248–3293, Jul. 2005.

[24] N. Ray, B. Kempf, T. Mützel, L. Froyen, K. Vanmeensel, and J. Vleugels, "Effect of WC particle size and ag volume fraction on electrical contact resistance and thermal conductivity of Ag–WC contact materials," *Mater. Des.*, vol. 85, pp. 412–422, Nov. 2015.

[25] M. Razavi, Y. S. Muzychka, and S. Kocabiyik, "Review of advances in thermal spreading resistance problems," *J. Thermophys. Heat Transf.*, vol. 30, no. 4, pp. 863–879, Oct. 2016.

[26] H. Hertz, "Über die berührung fester elastischer körper," *J. Reine Angew. Math.*, vol. 92, pp. 156–171, Nov. 1882.

[27] R. S. Timsit, "Electrical contact resistance: Properties of stationary interfaces," *IEEE Trans. Compon. Packag. Technol.*, vol. 22, no. 1, pp. 85–98, Mar. 1999.

[28] M. W. Denhoff, "An accurate calculation of spreading resistance," *J. Phys. D, Appl. Phys.*, vol. 39, no. 9, pp. 1761–1765, May 2006.

[29] S. Kristiansson, F. Ingvarson, and K. O. Jeppson, "Compact spreading resistance model for rectangular contacts on uniform and epitaxial substrates," *IEEE Trans. Electron Devices*, vol. 54, no. 9, pp. 2531–2536, Sep. 2007.

[30] J. A. Greenwood, "Constriction resistance and the real area of contact," *Brit. J. Appl. Phys.*, vol. 17, no. 12, pp. 1621–1632, Dec. 1966.

[31] M. Nakamura and I. Minowa, "Computer simulation for the conductance of a contact interface," *IEEE Trans. Compon., Hybrids, Manuf. Technol.*, vol. CHMT-9, no. 2, pp. 150–155, Jun. 1986.

[32] I. Minowa, M. Nakamura, and M. Kanno, "Conductance of a contact interface depending on the location and distribution of conducting spots," in *Proc. Elect. Contacts Electmech. Compon. Their Appl. Conf.*, 1986, pp. 19–28.

[33] J. F. Archard, "Single contacts and multiple encounters," *J. Appl. Phys.*, vol. 32, no. 8, pp. 1420–1425, Aug. 1961.

[34] B. J. Hamrock, *Fundamentals of Fluid Film Lubrication*. New York, NY, USA: McGraw-Hill, 1994.

[35] Y. Sano, "Effect of space angle of constriction resistance and contact resistance for the case of line contact," *IEEE Trans. Compon., Hybrids, Manuf. Technol.*, vol. 8, no. 1, pp. 228–234, Mar. 1985.
[36] H. Aichi and N. Tahara, "Analysis on the constriction resistance of the electric contact by the contact model using the electrolyte bath," in *Proc. 17th Int. Conf. Elect. Cont.*, Nagoya, Japan, Jul. 1994, pp. 1–7.
[37] A. Sharma and R. L. Jackson, "A finite element study of an elasto-plastic disk or cylindrical contact against a rigid flat in plane stress with bilinear hardening," *Tribol. Lett.*, vol. 65, no. 3, p. 112, Sep. 2017.
[38] R. L. Jackson, "A solution of rigid perfectly plastic cylindrical indentation in plane strain and comparison to elastic-plastic finite element predictions with hardening," *J. Appl. Mech.*, vol. 85, no. 2, Feb. 2018, Art. no. 024501.
[39] J. A. Greenwood and J. B. P. Williamson, "Contact of nominally flat surfaces," *Proc. R. Soc. Lond. A, Math. Phys. Sci.*, vol. 295, no. 1442, pp. 300–319, 1966.
[40] A. W. Bush, R. D. Gibson, and T. R. Thomas, "The elastic contact of a rough surface," *Wear*, vol. 35, no. 1, pp. 87–111, Nov. 1975.
[41] D. J. Whitehouse and M. J. Phillips, "Sampling in a two-dimensional plane," *J. Phys. A, Math. Gen.*, vol. 18, no. 13, pp. 2465–2477, Sep. 1985.
[42] J. Blanc, D. Grimme, and F. Blateyron, "Surface characterisation based upon signi?cant topographic features," in *Proc. 13th Int. Conf. Metrol. Prop. Eng. Surf.*, Twickenham, U.K., Apr. 2011, 012014.
[43] N. Yu and A. A. Polycarpou, "Extracting summit roughness parameters from random Gaussian surfaces accounting for asymmetry of the summit heights," *J. Tribol.*, vol. 126, no. 4, pp. 761–766, Oct. 2004.
[44] S. E. Rohde, A. I. Bennett, K. L. Harris, P. G. Ifju, T. E. Angelini, and W. G. Sawyer, "Measuring contact mechanics deformations using DIC through a transparent medium," *Exp. Mech.*, vol. 57, no. 9, pp. 1445–1455, Nov. 2017.
[45] H. Liu and J. W. McBride, "A Finite-Element-Based contact resistance model for rough surfaces: Applied to a bilayered Au/MWCNT composite," *IEEE Trans. Compon., Packag., Manuf. Technol.*, vol. 8, no. 6, pp. 919–926, Jun. 2018.
[46] C. Zhang, W. Ren, and F. Luo, "Understanding of the static contact behaviors of rod and spring for microelectromechanical relay," *IEEE Trans. Compon., Packag., Manuf. Technol.*, vol. 9, no. 12, pp. 2366–2373, Dec. 2019, doi: 10.1109/TCPMT.2019.2920143.
[47] C. Zhai, D. Hanaor, G. Proust, L. Brassart, and Y. Gan, "Interfacial electro-mechanical Behaviour at rough surfaces," *Extreme Mech. Lett.*, vol. 9, pp. 422–429, Dec. 2016.
[48] C. Zhai, Y. Gan, D. Hanaor, G. Proust, and D. Retraint, "The role of surface structure in normal contact stiffness," *Exp. Mech.*, vol. 56, no. 3, pp. 359–368, Mar. 2016.
[49] M. Mayer, M. Hodes, T. Kirk, and D. Crowdy, "Effect of surface curvature on contact resistance between cylinders," *J. Heat Transf.*, vol. 141, no. 3, Mar. 2019, Art. no. 032002.
[50] R. S. Timsit, "The potential distribution in a constricted cylinder," *J. Phys. D, Appl. Phys.*, vol. 10, no. 15, pp. 2011–2017, Oct. 1977.
[51] *Teledyne Electromechanical EMRs*. [Online]. Available: https://www.teledynerelays.com/Datasheets/J255.pdf

WANBIN REN (Member, IEEE) was born in 1977. He received the M.S. and Ph.D. degrees from the Harbin Institute of Technology, Harbin, China, in 2003 and 2006, respectively. He is currently a Professor with the School of Electrical Engineering and Automation, Harbin Institute of Technology. His current research interests include electrical contact theory and measurement techniques for electrical contact materials.

CHAO ZHANG was born in 1993. He received the B.S. degree from the Harbin Institute of Technology, China, in 2016, where he is currently pursuing the Ph.D. degree with the School of Electrical Engineering and Automation. His research interest is in static electrical contact behaviors of interconnectivity issues.

XILAI SUN, photograph and biography not available at the time of publication.